CIMAC CONGRESS 25
ZURICH, MAY 19 – 23, 2025

2025 | 127

The optimization of the structure of piston for ammonia-diesel dual-fuel engine under heavy load

Dual Fuel / Gas / Diesel

Yanling He, Tianjin University

Binyang Wu, Tianjin University
Zhenyuan Zi, Tianjin University
Minshuo Shi, Tianjin University
Tianshu Li, Tianjin University

ABSTRACT

As a zero-carbon fuel, ammonia represents one of the pathways for achieving zero-carbon emissions in internal combustion engines. However, high levels of unburned ammonia (UNHâ‚ƒ) emissions under high-load conditions result in low efficiency and pollution, which is one of the key challenges faced by ammonia-diesel dual-fuel (ADDF) engines. This study aims to achieve high ITEg and low UNHâ‚ƒ emissions in ADDF engines by employing a combined approach of bench testing and simulation modeling. The research focuses on the design and optimization of combustion chamber structures to reduce in-cylinder UNHâ‚ƒ emissions. By designing various combustion chamber configurations, the in-cylinder mixture formation and air motion were adjusted, resulting in improved combustion and reduced emissions. The engine was tested at a speed of 1,000 r/min, with IMEP of 18 bar, ammonia energy fraction of 80%, and a maintained compression ratio of 18.5 (consistent with the original engine). Several combustion chamber designs were explored. The results indicate that different combustion chamber structures significantly affect in-cylinder air motion and combustion. Higher swirl and tumble ratios promote better mixing of fuel and air, leading to slower combustion rates and reduced combustion efficiency. Compared with the original combustion chamber, the UNHâ‚ƒ emissions were reduced by 50.68%, 65.68%, and 69.74% for the double-round, hemisphere-round, and turbine-round, respectively, with corresponding increases in ITEg of 0.65%, 1.37%, and 2.08%. Additionally, the GHG were reduced by 19.23%, 28%, and 30.49%, respectively. These findings provide a reference for clean combustion and emission reduction in high substitution ratio ADDF engines.

1 INTRODUCTION

As the greenhouse effect worsens, carbon emissions from internal combustion engines, the main source of greenhouse gases in the transportation sector, have attracted increasing attention. Due to the low boiling point of hydrogen (20.28 K) and its high transportation costs, the storage and transportation of hydrogen face a series of challenges. Ammonia, as a carbon-free fuel and renewable energy source, is an efficient hydrogen carrier that can reduce carbon emissions from engine combustion. It is easy to transport, has low production costs, and aligns with current policy trends, giving it broad application prospects [1]. However, the high auto-ignition temperature, narrow flammability limit, and slow laminar flame speed of ammonia make it difficult to use as a standalone fuel [2,3], significantly hindering the development of pure ammonia engines. By employing dual-fuel combustion, ammonia can be mixed with highly reactive fuels such as diesel, dimethyl ether, hydrogen, or methane to overcome its shortcomings and substantially reduce carbon emissions [4]. The ammonia-diesel dual-fuel (ADDF) engine, which has shown significant potential in improving ammonia combustion, has become a research focus.

In 1966, Gray et al. conducted the first study on ADDF engines, demonstrating the combustion of ammonia at a relatively low compression ratio (15.2:1) [5]. Ickes et al. [6] found that the minimum compression ratio required for stable operation of dual-fuel engines depends on cetane number. With the intensification of the global greenhouse effect in the 21st century, the demand for carbon reduction and zero-carbon solutions has increased, reigniting interest in ammonia as an engine fuel.

Reiter et al. [7] studied the optimal operating range for dual-fuel operation of ADDF engines under various power modes on a four-stroke engine with a compression ratio of 17. The results showed that ammonia could be used as an alternative fuel in compression ignition engines. However, when the ammonia energy fraction (AEF) exceeded 60%, NO and unburned ammonia (UNH_3) emissions increased significantly, along with a prolonged ignition delay and a decrease in overall combustion rate. Wu et al. [8] investigated two pre-chamber ignition modes at high loads on a six-cylinder engine with a compression ratio of 18.5, showing that at an AEF of 50%, UNH_3 emissions decreased while thermal efficiency improved. However, with the AEF limited to 50%, there was no significant reduction in carbon emissions or greenhouse gas effects. Pei et al. [9] examined the effects of different combustion modes (PCCI and diesel-ignited ammonia) on UNH_3 emissions and thermal efficiency across multiple operating conditions on an engine with a compression ratio of 18.5. By adopting various injection strategies, they managed to control ammonia emissions to 6 g/(kWh) under medium to high load conditions with AEFs between 20%-60%, achieving thermal efficiencies comparable to pure diesel mode. However, at loads where diesel accounted for 40% or more of the fuel, carbon emissions remained high. Liu et al. [10] combined optical diagnostics with an adapted R425 diesel engine to study the effects of AEF and diesel injection strategies on combustion. With dual diesel injections, when the AEF reached 40%, there was a notable improvement in fuel mixing and flame propagation. However, at AEFs of 60%-80%, unburned regions increased, resulting in reduced combustion efficiency. Niki et al. [11,12] researched UNH_3 and N_2O emissions from ADDF engines using a 1.083L single-cylinder four-stroke engine. The study found that under high torque conditions, both UNH_3 and N_2O emissions increased with rising AEF, while thermal efficiency decreased. As load increased, higher in-cylinder temperatures helped reduce UNH_3 emissions. However, the AEF range in their study was limited to a maximum of 30%. Previous studies have explored various strategies to enhance the thermal efficiency of ammonia-diesel engines: adjusting the injection strategies of ammonia and diesel, installing pre-chambers to enhance jet turbulence within the cylinder, altering the in-cylinder compression ratio, or utilizing exhaust gas recirculation (EGR). However, these measures have not resolved the issue of high UNH_3 emissions and low thermal efficiency under high-load, high-substitution ratio conditions.

The configuration of the combustion chamber significantly impacts the in-cylinder combustion process and is an effective method for improving engine thermal efficiency and reducing emissions. Mittal et al. [13] investigated the effects of two combustion chamber geometries—bowl-in-piston and flat-piston—on combustion and emissions in a natural gas SI engine. The results showed that the bowl-in-piston combustion chamber exhibited higher thermal efficiency, while the flat-piston design achieved greater NOx reduction, demonstrating that different combustion chamber structures influence combustion and emissions in various ways. Huang et al. [14] used numerical simulations to study the effects of combustion chamber geometry and EGR on combustion and knock in a natural gas engine, finding that a turbine combustion chamber could generate stronger swirl and tumble, promoting in-cylinder mixing but increasing the tendency for knock. Wang et al. [15] experimentally and numerically modified the cylindrical combustion chamber of a natural gas engine by narrowing the chamber throat, investigating the effect of throat height on

combustion and thermal efficiency. The results showed that increasing the depth of the combustion chamber enhanced turbulence, shortened combustion duration, and improved thermal efficiency, but also heightened the risk of knock. Wohlgemuth et al. [16] proposed a novel design method and, through simulations, discussed the suitability of different geometries for a two-cylinder natural gas engine. The study demonstrated that a star-shaped combustion chamber could improve combustion, reduce fuel consumption, and enhance combustion stability, while reducing unburned hydrocarbon emissions under higher loads. Kurien et al. [17] addressed the low laminar combustion speed of ammonia by designing a stratified combustion chamber and adopting swirl enhancement techniques to improve the mixture distribution within the combustion chamber, thereby enhancing the performance of ammonia-diesel dual-fuel engines. Jones et al. [18] designed a swirling direct-injection diesel nebula combustion chamber for a single-cylinder engine, and experimental results indicated that this structure accelerated in-cylinder combustion, optimized emissions at the same fuel consumption, and improved ITEg.

Previous research has shown that altering the geometric structure of the combustion chamber can improve in-cylinder combustion and optimize emissions. As an effective measure for reducing carbon emissions and alleviating the energy crisis, ammonia-diesel engines are being widely studied for their efficiency and emissions. Despite extensive research [7-12], UNH_3 emissions and low thermal efficiency remain difficult issues to solve solely through injection strategies. This study addresses these challenges by optimizing the combustion chamber structure of an ammonia-diesel engine under high-load, high-substitution ratio conditions (AEF of 80%). By maintaining the in-cylinder compression ratio, we conducted a series of optimization studies on combustion chamber design to reduce UNH_3 emissions and improve combustion efficiency through structural changes that influence air motion within the cylinder. Ultimately, under an AEF of 80%, reductions in emissions and improvements in thermal efficiency were achieved.

2 Experimental Setup and Simulation Model Configuration

2.1 TEST BENCH AND EMISSION TESTING EQUIPMENT

This study was conducted using a modified Weichai WP10H heavy-duty diesel engine, with its main parameters listed in Table 1. The schematic diagram of the test bench is shown in Figure 1. Cylinder 6 of the engine was used as the test cylinder, while cylinders 1-5 remained unchanged and primarily served to provide the necessary engine speed for the test cylinder.

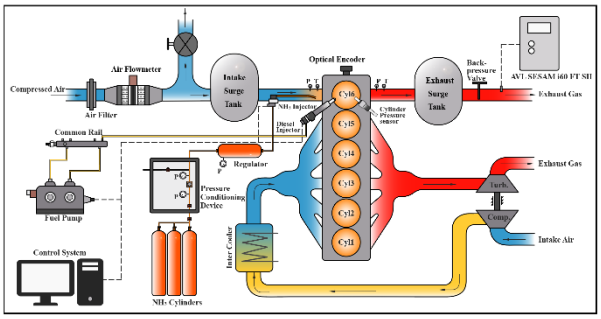

Fig. 1. Schematic of the diesel-ammonia dual-fuel engine test platform.

The single-cylinder engine had an independent intake system and fuel supply system. Ammonia was supplied by a high-flow ammonia delivery device, where it was depressurized through a pressure regulator and injected into the intake manifold via a gas injector, mixing with air before entering the cylinder. Diesel was directly injected into the cylinder through an injector in the main combustion chamber. In addition, the single-cylinder engine was equipped with an external intake boost simulation system (including an air compressor, air dryer, intake flow meter, and intake heating thermostat system), ensuring stable intake humidity, intake temperature, and intake flow for each cycle. These parameters could also be adjusted within a certain range.

Table 1 Engine parameters

Parameters	Value
Bore × stroke /mm	116×150
Connecting rod length /mm	224.5
Compression ratio	18.5:1
Displacement /L	1.56
Maximum combustion pressure /MPa	24
Ammonia injection mode	Port-injection
Ammonia injection pressure /bar	6
Combustion chamber type	ω
Number of holes × diameter /mm	8×0.169

2.2 COMBUSTION MODEL AND CHEMICAL REACTION MECHANISM

The chemical reaction mechanism used in the simulation model was developed and validated by Jin et al. [19] for ADDF combustion. This mechanism includes the n-heptane sub-mechanism developed by Zhang et al. [20], the NH_3 sub-mechanism developed by Shrestha et al. [21], and the NH_3/C1-C2 sub-mechanism developed by Glarborg et al. [22]. Based on these, the n-heptane sub-mechanism

was further simplified by integrating it with the NH_3 sub-mechanism and the NH_3/C1-C2 sub-mechanism. After adjusting certain reaction coefficients, a simplified chemical kinetic mechanism was obtained, containing 358 species and 2096 reaction steps. The ignition delay, flame speed, and species concentrations predicted by this mechanism were compared with experimental data, demonstrating its capability to accurately predict the chemical reactions in ADDF combustion.

Diesel, a typical liquid fuel, undergoes processes such as atomization, evaporation, and collision with the cylinder walls before combustion after being injected into the cylinder at high pressure. The combustion model employed the SAGE chemical reaction solver integrated within CONVERGE, using the ADDF chemical reaction mechanism developed by Jin et al. The sub-models for the CFD numerical simulations are shown in Table 2.

Table 2 Sub-model of CFD numerical simulation

Physical models	Selection
Turbulence model	RNG κ-ε
Breakup model	KH-RT
Evaporation model	Frossling
Collision model	NTC
Spray-wall interaction	Wall film
Combustion model	SAGE chemical reaction solver
Wall heat transfer model	Han & Reitz heat transfer

A three-dimensional physical simulation model was built in CONVERGE, as shown in Figure 2. Adaptive mesh refinement and grid division were applied, with a base mesh size of 4 mm. The original ADDF single-cylinder engine model was calibrated based on suitable turbulence models, diesel spray models, combustion models, heat transfer models, and chemical reaction mechanisms. The test conditions chosen for this study were a high-load condition with a speed of 1000 rpm and an IMEPg of 18 bar, with the fuel injection timing fixed at -10 °CA ATDC. To ensure simulation accuracy, calibration was conducted for both pure diesel and 80% AEF operating conditions. The boundary parameters for the calibrated conditions are listed in Table 3. Figure 3 compares the simulation results with experimental data, showing good agreement in both cylinder pressure and heat release rate curves, with a cylinder pressure peak error of less than 0.5%. Therefore, the model can effectively simulate the in-cylinder combustion process.

Table 3 Boundary parameters of the model calibration process

Parameters	0AEF(0A100D)	80%AEF(80A20D)
Engine speed /(r/min)	1000	
Cycle diesel mass/(mg/cycle)	140	28
Injection time/(° CA ATDC)	-10	
Compression ratio	18.5	
Diesel Injection Pressure /MPa	80	
Intake temperature /K	330	
IMEP /MPa	0.18	
Intake valve closing time/(° CA ATDC)	-150	
Exhaust valve open time/(° CA ATDC)	129	
EGR ratio	0	

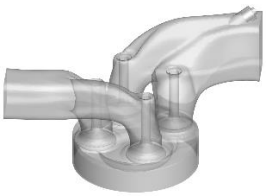

（a）Three-dimensional CFD model.

（b）Piston

Fig.2. Three-dimensional model of single-cylinder engine

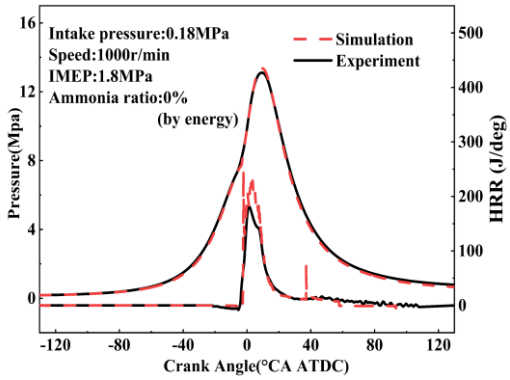

（a）0A100D

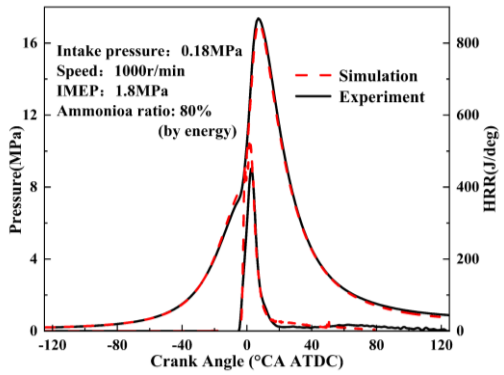

（b）80A20D

Fig. 3. Calibration of cylinder pressure and HRR curves in 3D simulation and test conditions

3 Combustion Chamber Structure Optimization and Methodology

The current ammonia-diesel mechanism was calibrated against the original engine model, and the pure diesel and ammonia-diesel operation under this mechanism demonstrated high consistency, meeting the required error margins. Based on these results, the study investigated the characteristics of unburned ammonia (UNH_3), power output, and emissions under different combustion chamber geometries.

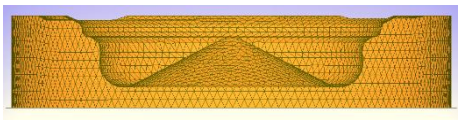

(a)

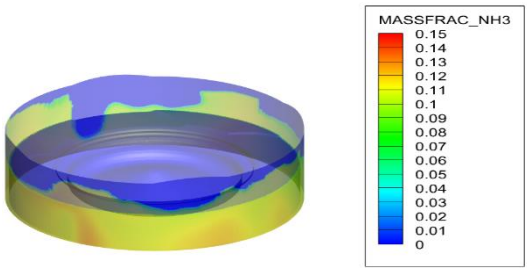

(b)

Fig. 4. (a) 2D diagram of the original (b) AEF=80% distribution of UNH3 in the cylinder at CA90 under a large load of 1000r/min

In this study, the compression ratio of the ADDF engine was kept constant at 18.5. When the ammonia energy fraction (AEF) was set at 80%, the experimental UNH_3 emissions were 23.45 g/(kWh). The calibrated simulation model predicted unburned ammonia emissions of 22.85 g/(kWh), with the calibration error being within 5%. The spatial distribution of unburned ammonia in the cylinder is shown in Figure 4. It can be observed that, in the later stages of combustion, a high concentration of unburned ammonia accumulates around the cylinder wall and piston ring crevice. Optimizing the fuel injection strategy alone is insufficient to reduce the unburned ammonia emissions in this region. However, modifying the combustion chamber structure can optimize in-cylinder flow dynamics, thereby improving flame propagation[23] and emission characteristics[24].

The structure of the combustion chamber significantly affects turbulence intensity, which in turn influences flame propagation. A concave combustion chamber shape promotes squish flow, enhancing the mixing of fuel and air at top dead center, but it does not easily form tumble flow, resulting in relatively low turbulence intensity in the combustion chamber. Additionally, the low laminar flame speed of ammonia makes it difficult for the flame to reach the crevice regions of the combustion chamber, where ammonia remains unburned. To address these issues, this study employed a design that incorporated inward protrusions on the sidewalls of the combustion chamber or eccentric arrangements to disrupt large-scale swirl flows and generate stronger turbulence. Five different combustion chamber geometries were designed to explore optimization methods and assess the impact of these structures on combustion and emissions, including unburned ammonia. The optimized combustion chamber models are shown in Figure 5[25-27]. Three-dimensional simulations were conducted for the optimized combustion chambers under the same model and boundary conditions as the original engine. The optimized results will be discussed in the following sections.

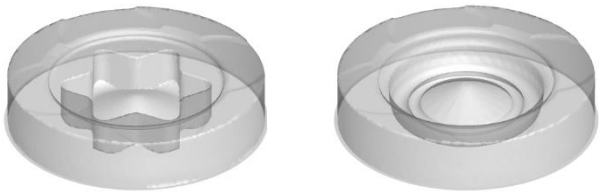

(a)star (b)double

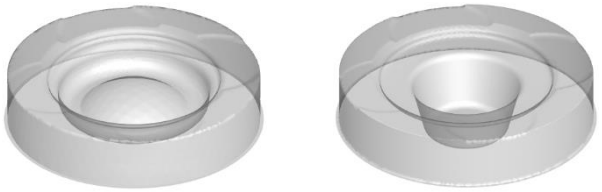

(c)hemisphere (d)turbine

(e)reentrant

Figure 5. Preliminarily optimized 3D diagram of the combustion chamber structure

4 Results and Discussion

4.1 EFFECT OF COMBUSTION CHAMBER STRUCTURE ON ENGINE COMBUSTION PERFORMANCE

Figure 6 shows the cylinder pressure and heat release rate (HRR) for different combustion chamber models. After optimization, five combustion chamber shapes were developed: star-shaped, double-shaped, hemisphere-shaped, turbine-shaped, and reentrant structures. Among these optimized combustion chambers, only the hemisphere structure exhibited higher pressure than the original model, while the pressures of the other optimized structures were generally lower than the original model. The intensity of the HRR peak was proportional to the pressure, as the hemisphere model facilitated better in-cylinder air-fuel mixing, resulting in improved combustion performance after initial optimization. From the HRR curves, it is evident that the HRR for the optimized cases fluctuated significantly with a delayed crank angle, and the timing of the HRR peak also showed notable changes. For the star, turbine, and reentrant combustion chambers, their longer chamber lengths resulted in weaker squish flow and uneven in-cylinder mixing. After diesel was initially ignited, the flame propagated and ignited the ammonia, causing the HRR peak to occur earlier, with a longer combustion duration and greater HRR fluctuations. On the other hand, the hemisphere combustion chamber had a shorter length, and the diesel, after being injected, was subjected to lateral compression along the combustion chamber, resulting in a longer mixing time. This led to a more uniform mixing of the fuel with in-cylinder gases, causing a delayed HRR peak and a higher heat release rate.

Figure 7 presents the various heat loss statistics and thermal efficiency for the different combustion chamber models. The indicated thermal efficiency (ITEg) of the original engine was 45.2%. Among the initially optimized combustion chambers, the hemisphere combustion chamber exhibited the highest ITEg at 45.1%, primarily due to its lower combustion and exhaust losses.

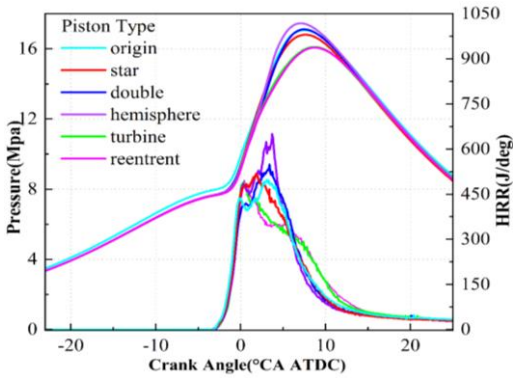

Fig.6. Pressure and HRR

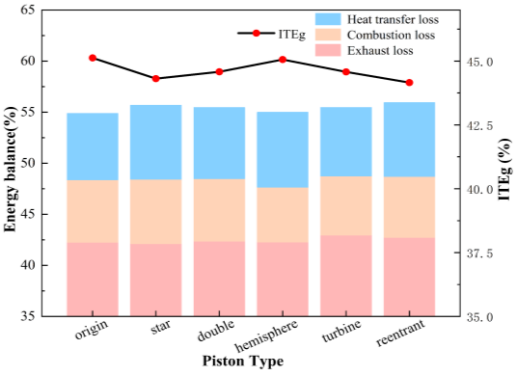

Fig.7. Energy balance and ITEg of different combustion chambers

Figure 8 presents the TKE (turbulent kinetic energy) and velocity distributions for different combustion chamber structures. Among the optimized combustion chamber models, the hemisphere and turbine chambers showed more vortices in the streamlines. Both the hemisphere and turbine chambers have the narrowest longitudinal and lateral spaces, and the compressed airflow striking the walls generated broken vortices, resulting in stronger airflow motion. This improved in-cylinder mixing and promoted faster flame propagation. The enhanced in-cylinder mixing and combustion process reduced the UNH3 emissions in these two combustion chamber configurations, leading to an increase in ITEg. In the reentrant and double combustion chambers, strong airflow was observed around the bottom of the piston and fuel plumes before ignition, intensifying as the piston moved to TDC (top dead center). However, no new vortices were generated in either configuration. Near TDC, the intense in-cylinder airflow helped propagate the flame into the chamber crevices, burning part of the ammonia trapped in the gaps. As the piston moved to CA50 (the point of 50% mass fraction burned), the cylinder volume expanded and the compression weakened, causing airflow to remain strong only within the combustion chamber. The diminished flame propagation in the weaker airflow

regions left residual UNH3 in the chamber crevices.

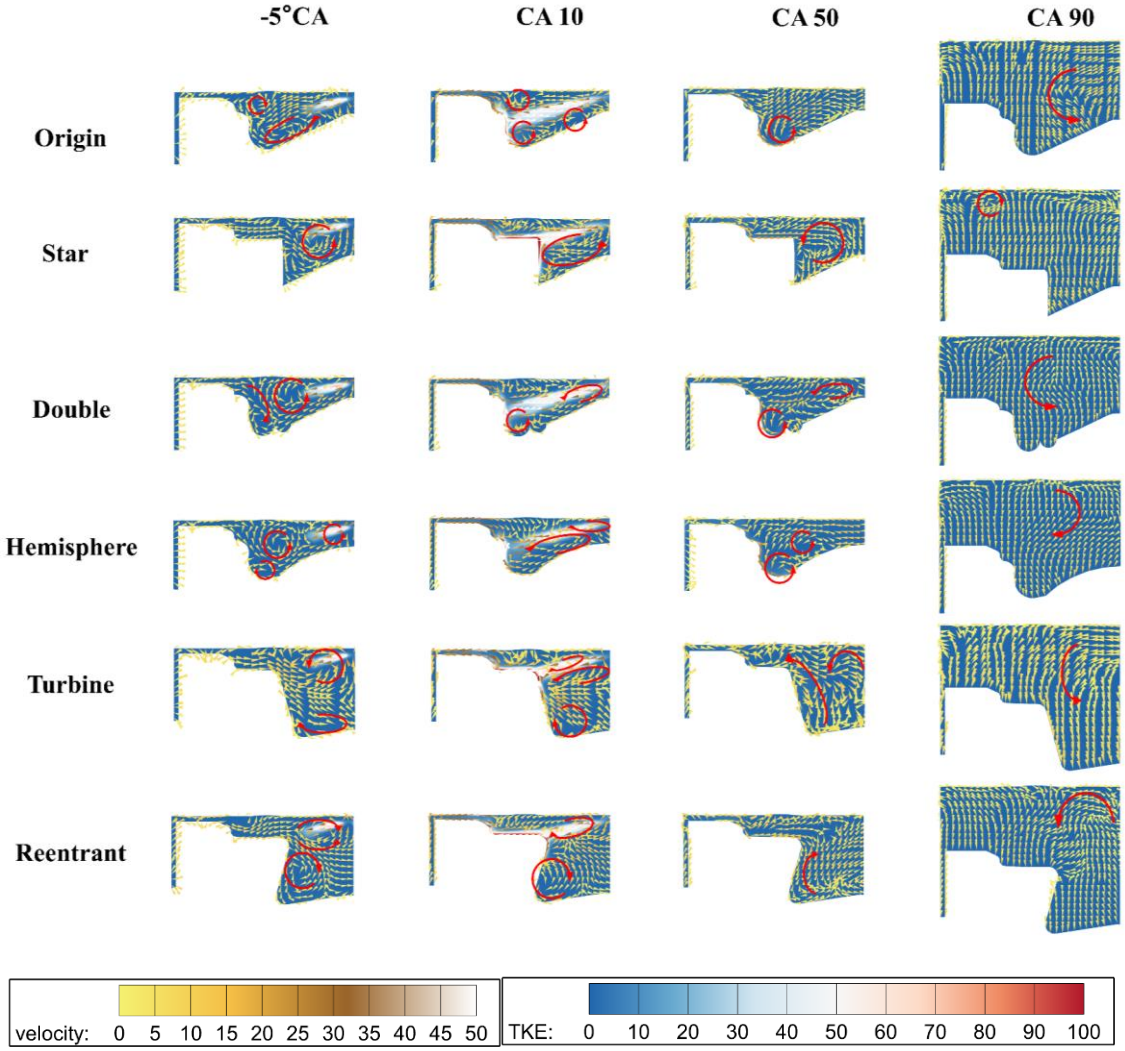

Fig.8. TKE and velocity in different combustion chambers

4.2 EFFECT OF COMBUSTION CHAMBER STRUCTURE ON THE COMBUSTION PROCESS

To further analyze the influence of different combustion chamber structures on combustion and emissions, Figure 9 shows the variation curves of swirl ratio, tumble ratio, and TKE with crank angle. The swirl ratio in the hemisphere combustion chamber was higher than that of the original model. During compression, the tumble ratio was relatively weak, but during the expansion stroke, the tumble ratio fluctuated dramatically, indicating intense in-cylinder motion. The hemisphere model had the highest TKE among the optimized configurations, and the flame rapidly propagated through the cylinder, continually entraining unburned gas into the flame front and accelerating combustion. Due to the longer combustion duration, heat loss was relatively high, which, despite its improved in-cylinder flow and combustion, caused the ITEg to be slightly lower than the original model.

The double combustion chamber, with a stratified structure, exhibited weaker swirl and tumble but slightly enhanced TKE. Although the in-cylinder airflow was relatively weaker, its ITEg was second only to the hemisphere model, achieving 44.5%. This is because, despite reducing in-cylinder flow and increasing combustion losses, the double chamber also reduced heat transfer, allowing its ITEg to remain relatively high.

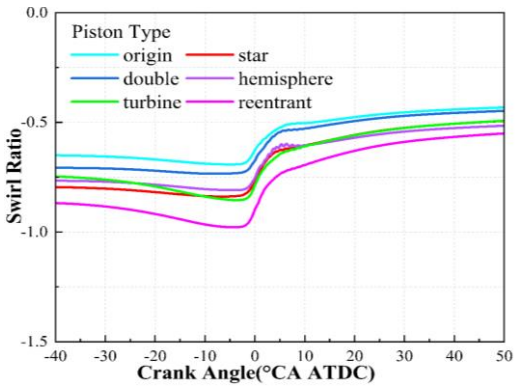

(a) Swirl Ratio

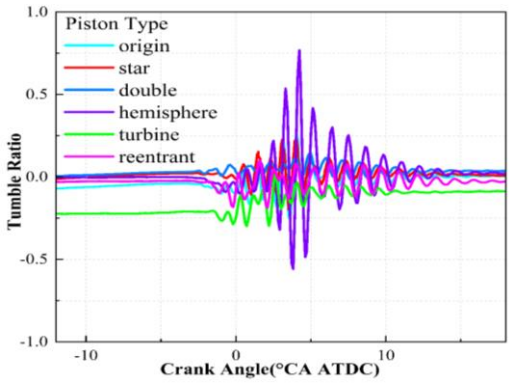

(b) Tumble Ratio

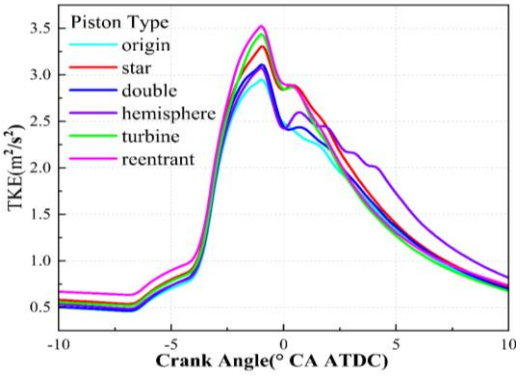

(c) TKE

Fig.9. (a)Swirl Ratio (b)Tumble Ratio (c) TKE in different combustion chambers

Figure 10 shows the in-cylinder temperature distribution at various combustion phases for different combustion chambers. In the turbine chamber, the flame propagated along the jet direction after ignition, and at CA50, the in-cylinder temperature was highest in the turbine configuration. During compression, diesel injection created strong vortex rotation in the cylinder, with a higher overall tumble ratio. The rapid mixing of fuel and air indicated that the turbine combustion chamber maximized in-cylinder space utilization, shortened the combustion duration, and reduced heat transfer losses.

In the star chamber, the turbulence level during compression was slightly lower than in the turbine chamber, and the tumble was weaker. However, as the TDC approached, the tumble ratio rapidly increased, and ignition occurred the fastest, with TKE peaking. Despite this, the star chamber had limited impact on the combustion process, and there was no significant improvement in in-cylinder flow, likely due to uneven air-fuel mixing in the earlier phases. Ammonia accumulated in the chamber gaps, and after ignition, weak in-cylinder flow only ignited the diesel, while the flame had difficulty propagating into the crevices to burn the ammonia. Consequently, the combustion performance of the star chamber was similar to that of the double chamber.

The reentrant combustion chamber exhibited the highest swirl ratio, with tumble fluctuations near the TDC, and also the largest TKE. Its in-cylinder flow characteristics were more favorable for flame propagation, with the in-cylinder temperature at CA50 being second only to the turbine chamber. However, due to the narrow chamber sidewalls, airflow had difficulty penetrating into the combustion chamber gaps. The reentrant chamber had lower combustion losses compared to the star and double configurations, and its in-cylinder flow was the most optimal. However, it had higher exhaust losses, resulting in an ITEg of only 44.1%. Further optimization is needed to reduce exhaust losses based on this structure.

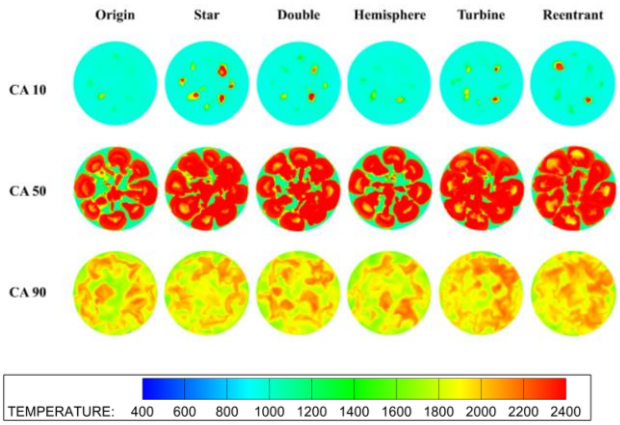

Fig.10 Temperature contours of different combustion chambers at CA10, CA50 and CA90

4.3 Effect of Combustion Chamber Structure on Engine Emission Performance

Figure 11 shows the CO2 and GHG emissions for different combustion chamber structures. The turbine chamber had the lowest CO2 emissions at 102.13 g/kWh, a reduction of 8.89% compared to the original model. This chamber structure promoted more complete diesel combustion. However, the turbine chamber had a 5.38% higher GHG emission than the original model, primarily due to increased N2O emissions. The star chamber had the lowest GHG emissions at 164.21 g/kWh, 8.2% lower than the original model, with CO2 emissions similar to the baseline. Among the optimized models, the double chamber had the weakest GHG reduction, only reducing emissions by 1.22% compared to the original model, with CO2 emissions remaining unchanged. High GHG

emissions in the double chamber were dominated by N2O, highlighting the reduction of N2O as a key goal in combustion chamber optimization.

Figure 12 displays UNH3 and NOx emissions for different combustion chamber structures. Reducing UNH3 emissions is critical to improving the indicated thermal efficiency of ADDF engines. The hemisphere chamber achieved the highest ITEg and the lowest UNH3 emissions, as its high combustion efficiency and improved in-cylinder flow allowed the flame and gas mixture to penetrate the chamber gaps, reducing UNH3 emissions, as shown by the 1500 K isothermal surface in Figure 13. The star chamber had the highest UNH3 emissions and the lowest thermal efficiency at 44.3%. The double and turbine chambers had similar UNH3 emissions and efficiency levels, with NOx emissions of 7.36 g/kWh and 6.29 g/kWh, respectively, though both had higher GHG emissions than the original model. In summary, the hemisphere chamber demonstrated excellent in-cylinder flow and combustion performance, achieving high thermal efficiency. In terms of emissions, the turbine chamber had low UNH3 and NOx emissions.

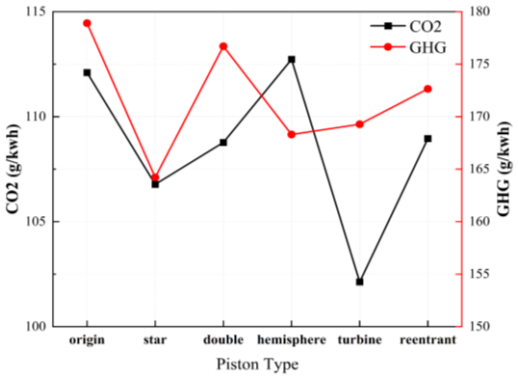

Fig. 11. GHG and CO2 emissions in different combustion chambers

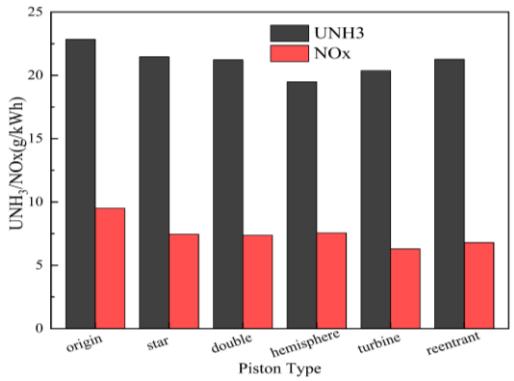

Fig. 12. Emissions of UNH3 and NOx in different combustion chambers

Figure 13 illustrates the in-cylinder distribution of UNH3 at various crank angles, along with the 1500 K isothermal surface. In the original model, UNH3 was concentrated in the piston-side crevices. After initial optimization, the turbine combustion chamber achieved the most uniform in-cylinder distribution of NH3, with minimal accumulation in the crevices, resulting in a UNH3 mass fraction of about 10%. Other chambers also exhibited more uniform in-cylinder distributions of NH3, but the change in UNH3 emissions was not significant, with mass fractions around 12%, still concentrated in the combustion chamber crevices. While the optimizations improved in-cylinder flow and impacted pollutant emissions, further refinements are necessary. Near the TDC, high in-cylinder pressure and strong flow allowed the flame to propagate into the crevices, burning part of the trapped UNH3. However, as the piston moved away from TDC and the in-cylinder volume increased, airflow weakened, and the flame propagation lost momentum, leaving residual UNH3 in the combustion chamber gaps. Based on this analysis, the narrow sidewall gaps in the combustion chamber restricted flame penetration, causing excessive UNH3 emissions. Optimizing the sidewall design could allow the flame to burn NH3 more effectively within the crevices.

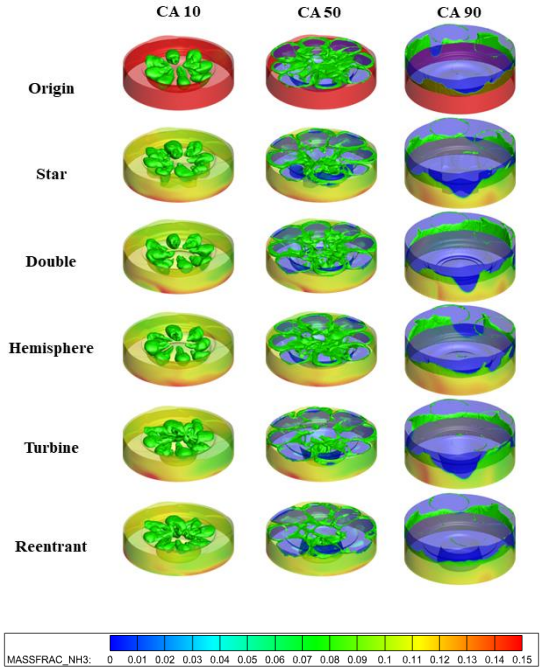

Fig.13 The distribution of UNH3 in the cylinder at CA10、CA50、CA90 and the 1500K isosurface

4.4 FURTHER IMPROVEMENTS TO COMBUSTION CHAMBER DESIGN

Although the previous optimizations of the combustion chamber partially improved the in-cylinder flow and combustion, the issues of high

UNH3 emissions and low engine thermal efficiency remain unresolved. Analysis of the combustion process reveals that, while the in-cylinder structure affects flow and combustion, UNH3 still concentrates in the piston ring crevice. The narrow space in this area prevents flame propagation, resulting in incomplete combustion of the fuel mixture. To address this issue, further optimization was carried out based on the initial modifications.

As shown in Figure 14, the combustion chamber was re-optimized. Building on the initial optimizations, the sidewall of the combustion chamber was redesigned to address the accumulation of UNH3 in the piston ring crevice. The sidewall was modified to incorporate a hemispherical section, while maintaining the same compression ratio. After optimization, in-cylinder combustion was significantly improved, and UNH3 concentration in the piston ring crevice was reduced, leading to further improvements in engine thermal efficiency.

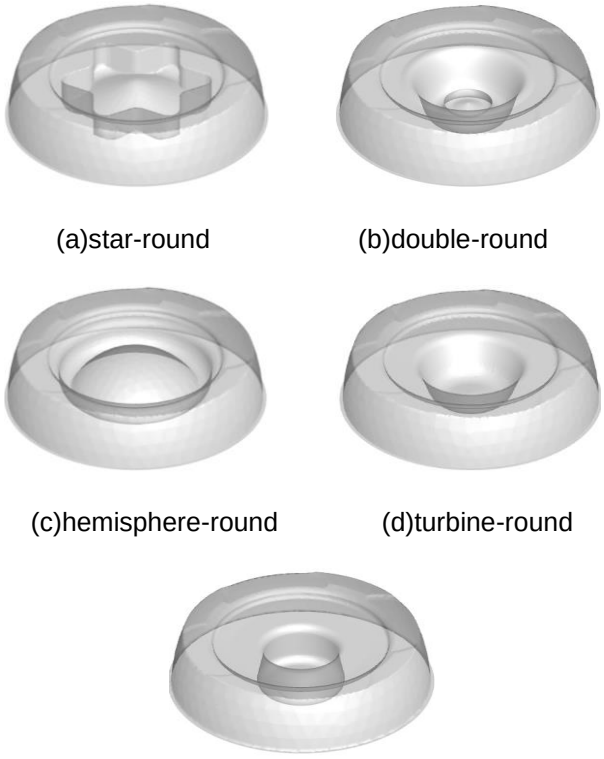

(a)star-round (b)double-round

(c)hemisphere-round (d)turbine-round

(e)reentrant-round

Fig.14. The structure of the re-optimized combustion chamber model

The pressure and heat release rate (HRR) of the optimized combustion chambers are shown in Figure 15. The peak cylinder pressure in the optimized models was reduced and delayed. This is because, when the swirl ratio is between 0 and 1, a higher swirl ratio results in the air-fuel mixture being carried to more distant areas, leading to overly homogeneous fuel mixing and an increased combustion duration. The HRR of the optimized combustion chambers exhibited two peaks: the first occurred near the top dead center (TDC), representing premixed combustion, while the second appeared around 6° CA ATDC, representing diffusion combustion—phenomena not observed in the original model. In the original model, combustion duration was long and the fuel-air mixture was relatively uniform, thus lacking the dual peaks. The widened sidewall of the optimized combustion chamber improved fuel-air mixing and flame propagation. Since the swirl ratio in the secondary optimization was smaller than in the initial optimization, flame propagation was less influenced by in-cylinder flow. This resulted in a premixed combustion HRR peak forming near the TDC, followed by a diffusion combustion HRR peak due to the continuous injection and combustion of diesel fuel after ignited.

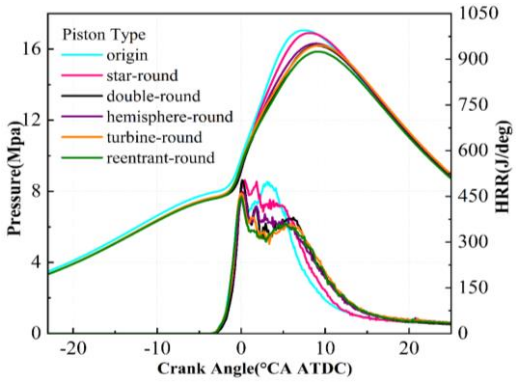

Fig.15. Cylinder pressure and HRR after re-optimized

Figure 16 shows the exhaust losses, heat transfer losses, combustion losses, and combustion duration of the optimized combustion chambers. Among the five optimized designs, the combustion durations of the double-round, hemisphere-round, and turbine-round chambers were shorter than those of the original model, and the ITEg was improved by 0.65%, 1.37%, and 2.08%, respectively. Of these, the turbine-round chamber achieved the highest thermal efficiency, reaching 46.1%. This improvement is mainly due to the turbine-round chamber's low UNH3 emissions, which were reduced to 6.907 g/(kWh), representing a 69.74% reduction compared to the original model (Figure 17). All three of these optimized chambers exhibited slightly higher exhaust losses than the original model, but significantly lower combustion losses, and comparable heat transfer losses, ultimately resulting in higher thermal efficiency. In contrast, the reentrant-round chamber had the longest combustion duration and the lowest ITEg, at only 44.75%. It also had the highest UNH3 emissions, at 12.79 g/(kWh). The high combustion losses in the reentrant-round chamber led to its low

thermal efficiency, which was 0.81% lower than the original model. This is because the in-cylinder flow in the reentrant-round design was not as strong as in the turbine-round and hemisphere-round designs (as shown in Figure 19), and therefore, the in-cylinder flow did not adequately propagate to the sidewall. Consequently, the weak flow near the sidewall hindered flame propagation, leading to incomplete combustion of UNH3 and higher emissions in the reentrant-round chamber.

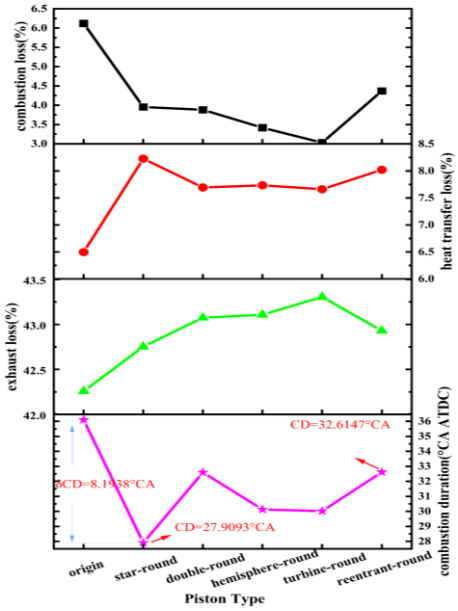

Fig.16. Combustion loss and CD after combustion chamber optimization

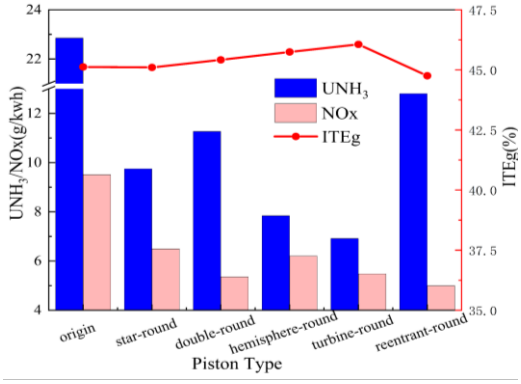

Fig. 17 UNH3 emissions and efficiency after optimization of different combustion chambers

Figure 18 presents contour maps of UNH3 distribution within the cylinder at various crank angles and 1500 K iso-surfaces following the optimization of the sidewall structure. Compared to the initial optimization, the re-optimized combustion chamber exhibited significantly stronger flames near the TDC, and at CA 5, the flame began to propagate toward the combustion chamber sidewall, as shown in the comparison with Figure 14 at the same moment. Due to the optimization of the combustion chamber sidewall structure, the air-fuel mixture was more evenly mixed, and the flame propagated more efficiently, combusting UNH3 near the sidewall. During the mid to late combustion phase (CA = 20° CA ATDC), as seen from the 1500 K temperature distribution, the optimized combustion chamber allowed flame penetration into more than half of the sidewall gap, significantly reducing the amount of residual ammonia gas. In contrast, the flame in the initial optimization only propagated into less than one-third of the sidewall depth. This optimization successfully addressed the issue of narrow sidewall gaps impeding flame propagation, thus reducing the accumulation of unburned ammonia in the sidewall crevices. At CA90, combustion had largely ceased, leaving only a small amount of high-temperature gas. Except for the double-round combustion chamber, the concentration of UNH3 in the cylinder at this time was visibly lower than in Figure 13. The relatively high concentration of UNH3 was primarily confined to the bottom of the sidewall, while lower concentrations were observed in areas diffused from the high-concentration regions. The UNH3 distribution in the double-round chamber remained relatively dense, and its emissions reached 11.25 g/(kWh), which was higher than in the other optimized models. Figure 19 shows that, before the TDC, the in-cylinder swirl and tumble motions in the double-round chamber were weak. At the TDC, the in-cylinder flow moved toward the sidewall, but the flow was slow, and fewer eddies formed compared to the other chamber designs. After TDC, the sidewall optimization generated vortices above the sidewall, but the flow was still weaker than in the other models. Consequently, the fuel-air mixture near the sidewall was less homogeneous, and flame propagation was less efficient, leading to incomplete combustion and higher residual UNH3 emissions.

In the hemisphere-round and turbine-round chambers, numerous vortex structures had already formed before the compression to the TDC, promoting better mixing of air and fuel, and resulting in lower diesel fuel concentrations. This caused a slight delay in the ignition timing. After reaching the TDC, the in-cylinder flow compressed and broke up into smaller eddies, accelerating flame propagation and carrying the fuel-air mixture toward the combustion chamber sidewalls. As shown in Figure 19, these two models exhibited dense flow lines propagating from the cylinder to the sidewall gap, with many distinct vortices. After the piston moved downward, the in-cylinder flow moved outward, creating a strong reverse squish flow, which helped propagate the flame toward the sidewall and burn the NH3 in the gaps. This

overcame the challenges of slow flame propagation and difficult ignition under high substitution ratios. Therefore, the hemisphere-round and turbine-round combustion chambers exhibited superior combustion characteristics and lower UNH3 emissions.

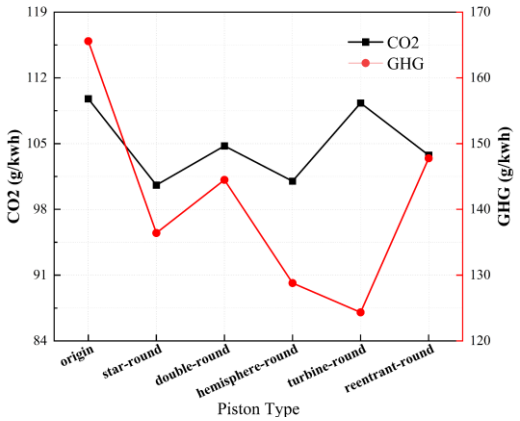

Fig.20 Optimized CO2 emissions and GHG after different combustion chambers were optimized on the sidewall surface

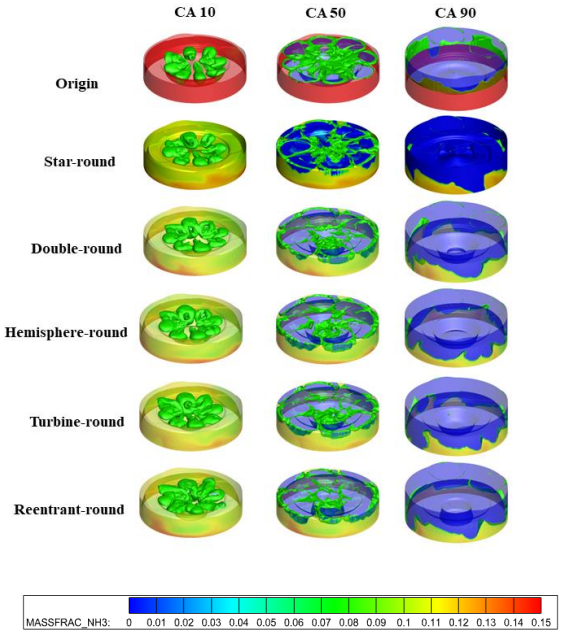

Fig.18. Distribution contour diagram of UNH3 in the cylinder at different crankshaft after sidewall surface optimization and 1500K isosurface

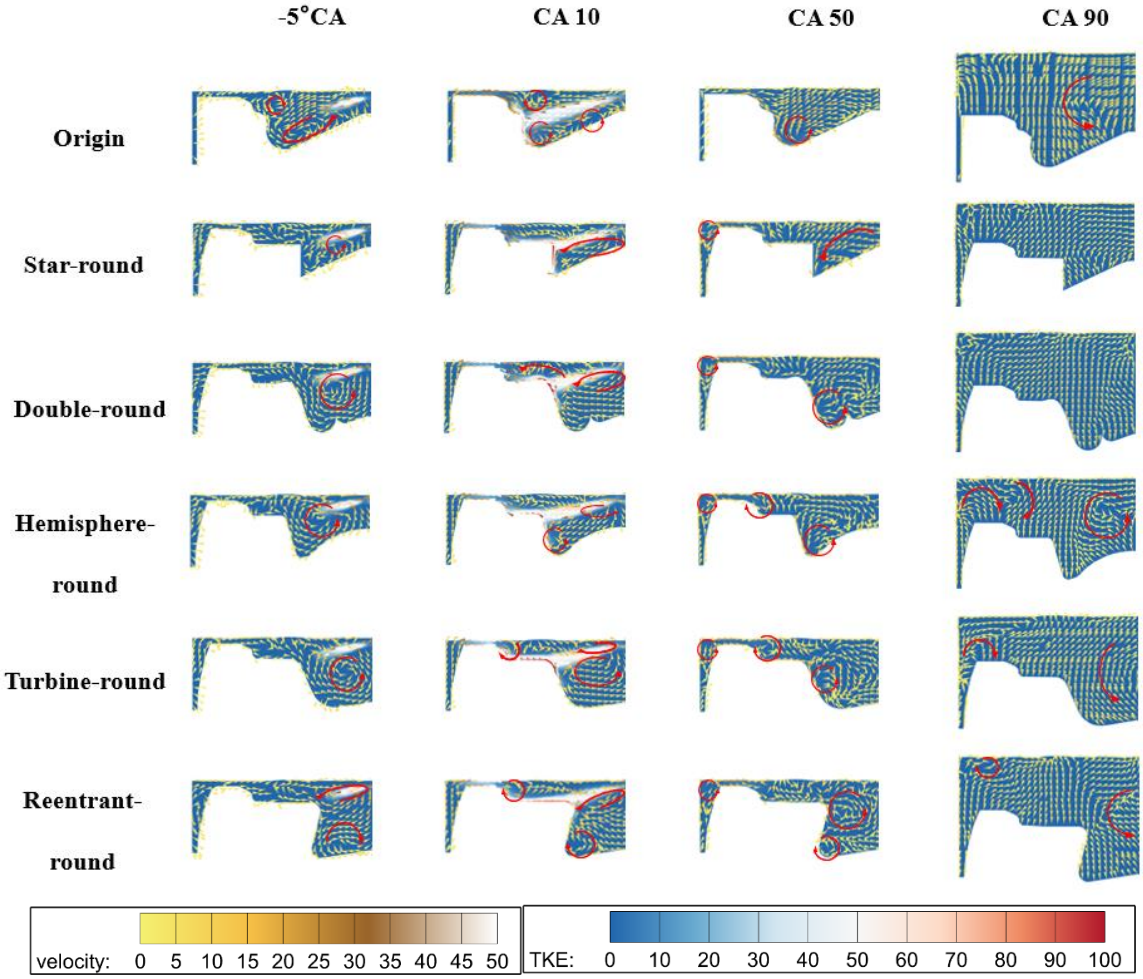

Fig.19. TKE and velocity in different combustion chambers after sidewall optimization

Figure 20 illustrates the CO2 and GHG emissions after optimizing the combustion chamber designs. The CO2 and GHG emissions of the optimized combustion chambers were all lower than those of the original model. The turbine-round chamber had the lowest GHG emissions, at 124.344 g/(kWh), but also the highest CO2 emissions among the optimized models, at 109.322 g/(kWh). The reentrant-round chamber had the highest GHG value, but it was still 17.4% lower than the original model, while its CO2 emissions were 7.43% lower than those of the original model. Thus, the optimized combustion chambers produced favorable results in terms of both carbon emissions and greenhouse gas effects.

5 CONCLUSIONS

To address the issues of high unburned ammonia emissions and low efficiency under high-load, high-substitution ratio conditions, a structural optimization study of the combustion chamber was conducted based on 3D combustion simulations. The study was performed at an engine speed of 1000 rpm and IMEP of 18 bar, analyzing in-cylinder flow and flame propagation. The main conclusions are as follows:

(1) For the initially optimized model, a stronger in-cylinder swirl and a higher tumble ratio near top dead center (TDC) resulted in higher thermal efficiency. The turbine combustion chamber produced the least UNH3 and NOx emissions, with minimal heat loss. After optimizing the sidewall of the combustion chamber, models with weaker in-cylinder flow near TDC exhibited less homogeneous fuel-air mixing and a double-peaked heat release rate (HRR). The faster combustion rate shortened the combustion duration and improved thermal efficiency.

(2) In the initially optimized model, geometric optimizations of the combustion chamber caused significant changes in in-cylinder flow and improved the combustion process. However, substantial amounts of UNH3 still accumulated on the sidewall surface. To address the problem of flame propagation being hindered by excessively narrow sidewall gaps, which led to NH3 accumulation, further optimization of the sidewall structure allowed the flame to penetrate the gaps, effectively combusting NH3 in these regions. This significantly reduced UNH3 emissions, with part of the unburned ammonia converted into useful work. Additionally, NOx emissions were reduced, and thermal efficiency improved.

(3) In the optimized turbine-round combustion chamber model, unburned ammonia emissions were reduced by 69.74%, with a corresponding 2.08% improvement in ITEg. Furthermore, GHG emissions decreased by 30.49%, and NOx emissions were reduced by 42.35%.

References and bibliography

[1] Deng LF, Hao CF, Luo YM, Yang PZ, Wu BY. Effect of air and exhaust gas dilutions on ultra-fine particulate emissions in different combustion modes. *Sci Total Environ* 2022;843:13.

[2] H. Nozari and A. Karabeyo\uglu, “Numerical study of combustion characteristics of ammonia as a renewable fuel and establishment of reduced reaction mechanisms,” *Fuel*, vol. 159, pp. 223–233, 2015.

[3] Lhuillier Charles, Brequigny Pierre, Contino Francesco, Mounaïm-Rousselle Christine. Experimental investigation on ammonia combustion behavior in a spark-ignition engine by means of laminar and turbulent expanding flames. Proc. *Combust*. Inst. 2021;38(4):5859–68.

[4] Caneon Kurien, Mayank Mittal, Review on the production and utilization of green ammonia as an alternate fuel in dual-fuel compression ignition engines, *Energy Conversion and Management*, Volume 251, 2022, 114990, ISSN 0196-8904.

[5] Gray, J., Dimitroff, E., Meckel, N., and Quillian, R., "Ammonia Fuel - Engine Compatibility and Combustion," *SAE* Technical Paper 660156, 1966, https://doi.org/10.4271/660156

[6] Ickes Andrew, Wallner Thomas, Zhang Yu, De Ojeda William. Impact of cetane number on combustion of a gasoline-diesel dual-fuel heavy-duty multi-cylinder engine. *SAE* Int. J. Engines 2014;7(2):860–72.

[7] Aaron J. Reiter, Song-Charng Kong, Combustion and emissions characteristics of compression-ignition engine using dual ammonia-diesel fuel, *Fuel*, Volume 90, Issue 1, 2011, Pages 87-97, ISSN 0016-2361.

[8] Binyang Wu, Minshuo Shi, Shouying Jin, Jiayong Wang, Zhenyuan Zi, Puze Yang, Qingyang Ma, Comparison and optimization of strategies for ammonia-diesel dual-fuel engine based on reactivity assisted jet ignition and reactivity turbulent jet disturbance under high load conditions, *International Journal of Hydrogen Energy,* Volume 67, 2024, Pages 487-499, ISSN 0360-3199.

[9] Yiqiang Pei, Decheng Wang, Shouying Jin, Yuncheng Gu, Chunling Wu, Binyang Wu, A quantitative study on the combustion and emission characteristics of an Ammonia-Diesel Dual-fuel

(ADDF) engine, *Fuel Processing Technology*, Volume 250, 2023, 107906, ISSN 0378-3820.

[10] Xu Liu, Qian Wang, Wenjun Zhong, Peng Jiang, Min Xu, Botian Guo, Optical diagnostics in impact of ammonia energy ratio and diesel split ratio on combustion process and flame propagation in an Ammonia-Diesel Dual-Fuel engine, *Fuel*, Volume 364, 2024, 131074, ISSN 0016-2361.

[11] Niki Y, Nitta Y, Sekiguchi H, Hirata K. Emission and Combustion Characteristics of Diesel Engine Fumigated With Ammonia. *ASME* 2018 Internal Combustion Engine Division Fall Technical Conference. Volume 1: Large Bore Engines; Fuels; Advanced Combustion. 2018.

[12] Niki Y, Nitta Y, Sekiguchi H, Hirata K. Diesel Fuel Multiple Injection Effects on Emission Characteristics of Diesel Engine Mixed Ammonia Gas Into Intake Air. *Journal of Engineering for Gas Turbines and Power* 2019;141(6).

[13] Penmatsa Sandeep Varma, Mayank Mittal. Investigations with bowl-in-piston (CI type) and flat-piston (SI type) geometries to study the engine characteristics of a CI engine retrofitted for SI operation with CNG fuel, *Energy Conversion and Management*, Volume 301, 2024, 118083, ISSN 0196-8904.

[14] Bin Liang, Lei Cheng, Meng Zhang, Yongcheng Huang, Jinhua Wang, Yongzheng Liu, Fanhua Ma, Zuohua Huang. Effects of chamber geometry, hydrogen ratio and EGR ratio on the combustion process and knocking characters of a HCNG engine at the stoichiometric condition, *Applications in Energy and Combustion Science*, Volume 15, 2023, 100189, ISSN 2666-352X.

[16] Wohlgemuth, S., Roesler, S., and Wachtmeister, G. Piston Design Optimization for a Two-Cylinder Lean-Burn Natural Gas Engine - 3D-CFD-Simulation and Test Bed Measurements. *SAE* Technical Paper 2014-01-1326, 2014, https://doi.org/10.4271/2014-01-1326

[17] Caneon Kurien, Mayank Mittal, Review on the production and utilization of green ammonia as an alternate fuel in dual-fuel compression ignition engines, *Energy Conversion and Management*, Volume 251, 2022, 114990, ISSN 0196-8904, https://doi.org/10.1016/j.enconman.2021.114990.

[18] Jones, M. and Heaton, D., Nebula Combustion System for Lean Burn Spark Ignited Gas Engines. *SAE* Technical Paper 890211, 1989, https://doi.org/10.4271/890211.

[19] Jin S, Wu B, Zi Z, et al. Effects of fuel injection strategy and ammonia energy ratio on combustion and emissions of ammonia-diesel dual-fuel engine[J]. *Fuel*, 2023,341:127668.

[20] Zhang KW, Banyon C, Bugler J, Curran HJ, Rodriguez A, Herbinet O, et al. An updated experimental and kinetic modeling study of n-heptane oxidation. *Combustion and Flame* 2016;172:116-35.

[21] Shrestha KP, Seidel L, Zeuch T, Mauss F. Detailed Kinetic Mechanism for the Oxidation of Ammonia Including the Formation and Reduction of Nitrogen Oxides. *Energy & Fuels* 2018;32(10):10202-17.

[22] Glarborg P, Miller JA, Ruscic B, Klippenstein SJ. Modeling nitrogen chemistry in combustion. *Progress in Energy and Combustion Science* 2018;67:31-68.

[23] Penmatsa Sandeep Varma, Mayank Mittal, Investigations with bowl-in-piston (CI type) and flat-piston (SI type) geometries to study the engine characteristics of a CI engine retrofitted for SI operation with CNG fuel, *Energy Conversion and Management*, Volume 301, 2024, 118083, ISSN 0196-8904.

[24] Nurullah Gültekin, Murat Ciniviz. Examination of the effect of combustion chamber geometry and mixing ratio on engine performance and emissions in a hydrogen-diesel dual-fuel compression-ignition engine, *International Journal of Hydrogen Energy*, Volume 48, Issue 7, 2023, Pages 2801-2820, ISSN 0360-3199.

[25] H. Reddy, J. Abraham, Ignition kernel development studies relevant to lean-burn natural gas engines, *Fuel* 89 (2010) 3262–3271.

[26] H. Cho, B. He, Combustion and emission characteristics of a lean burn natural gas engine, Int. J. *Automot. Technol*. 9 (2008) 415–422.

[27] Bowen Yan, Laihui Tong, Hu Wang, Zunqing Zheng, Yufeng Qin, Mingfa Yao. Experimental and numerical investigation of the effects of combustion chamber reentrant level on combustion characteristics and thermal efficiency of stoichiometric operation natural gas engine with EGR, *Applied Thermal Engineering,* olume 123, 2017, Pages 1473-1483, ISSN 1359-4311.